Gemini II: Design, Modeling, and Control of a Compact Yet Efficient Servoless Bi-copter

Youming Qin, Nan Chen, Yixi Cai, Wei Xu, and Fu Zhang, *Member, IEEE*

***Abstract*—Unmanned aerial vehicles (UAV) are widely used in the field for tasks that require 3-D movements in space. The simultaneous demand for heavy payload capacity, long operating time, and size restriction poses a challenge to UAV design. To solve this conundrum, this article proposes a novel bi-copter with only two actuators. Unlike tandem rotor bi-copters that utilize two servomotors to achieve yaw and roll control, our novel design, the Gemini II bi-copter, controls attitude by using cyclic flapping response in hinges that connect the blades. This passive cyclic pitch-varying mechanism makes the UAV no longer depend on two heavy and expensive servo motors or swashplate to vector the thrust. This change of propulsion system not only makes the UAV mechanically simpler, more reliable, and cost-effective, but also enhances the UAV performance by mitigating the issues of backlash, nonlinearity, and nonminimum phase caused by servo motors. To the best of the authors' knowledge, the Gemini II, built entirely on off-the-shelf electronics, is the first servoless bi-copter that can precisely control its 3-D position and orientation with two actuators only. To demonstrate the flight performance and applications of the proposed novel UAV, we conduct path-following experiments along with manual poking and wind disturbances tests.**

***Index Terms*—Aerial robotics, bi-copter, field robotics, indoor UAV, swashplate-less, UAV control.**

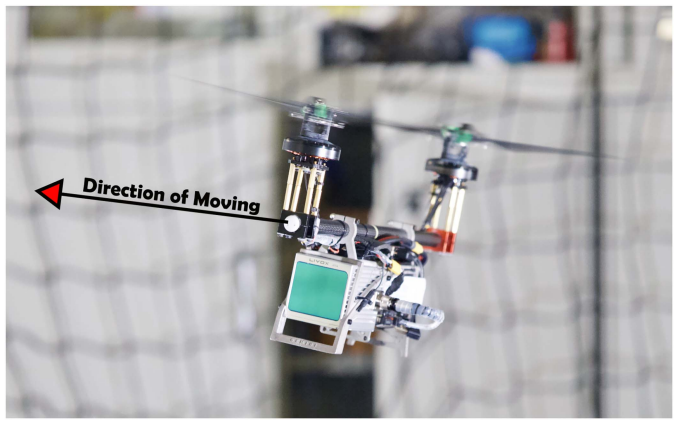

Fig. 1. Gemini II servoless bi-copter performing agile maneuvering. The propeller size is 13 in. The Gemini II moves in the direction indicated by the arrow, and it is able to control its attitude with the cyclic blade pitch control technique. It carries a front-facing 3-D LiDAR and an onboard computer, which makes it able to perform tasks like real-time 3-D LiDAR mapping. With a take-off weight of 1.87 kg and 13-in propellers, our exemplary design Gemini II carries a 600-g LiDAR while only consuming 193 W of power, resulting in 22 min of operation time. Video is available in the supplementary material at https://youtu.be/qGhQbPtp7Sw.

I. Introduction

MULTIROTOR unmanned aerial vehicles (UAVs) have been used for the primary data-gathering tasks such as indoor construction site mapping, soil inspection, and postdisaster search and rescue [1]–[4]. During those tasks, the UAVs usually have to carry heavy payloads and navigate in confined spaces. As a result, there is a demand for maximizing efficiency while minimizing the UAV size [5].

As the most common multirotor UAV platform, the quadcopter is able to roll its whole body into narrow gaps, thanks to its flat geometry [6], [7]. But this approach limits its payload capacity and cannot be sustained for long. The morphing approach in [8]–[10] increases the mechanical complexity and weight, making the platform less efficient and unreliable.

According to the ideal disk loading theory, a lower disk loading (thrust generated per unit area of the rotor disc) results in higher hovering efficiency [11]. Based on the theory, Qin *et al.* [12] showed that given the same width limit, the bi-copter platform is the most power-efficient yet practical (in terms of mechanical simplicity) solution among 12 common practical rotor configurations. Traditional large bi-copters like Boeing CH-47 achieve control over their cyclic pitch by using a swashplate mechanism. However, such a mechanism is expensive, heavy, bulky, and requires constant maintenance [13]. This complicated swashplate mechanism also poses a tremendous challenge for flight control and is rarely used in low-cost small UAVs. By using servo motors to achieve tilting of each individual propeller for yaw and roll control, the tandem tilt-rotor configuration is a more practical solution for indoor applications and has been widely explored by researchers [12], [14]–[20]. Likewise, Siddhardha [21] uses reaction wheels to maintain a similar level

Manuscript received 29 August 2021; revised 20 December 2021; accepted 30 January 2022. Date of publication 16 March 2022; date of current version 14 December 2022. Recommended by Technical Editor Y. Shtessel and Senior Editor M. Basin. This work is supported in part by a DJI donation and in part by the HKU startup fund for new staff. *(Youming Qin and Nan Chen are co-first authors.) (Corresponding author: Fu Zhang.)*

The authors are with the Department of Mechanical Engineering, University of Hong Kong, Hong Kong (e-mail: qym96@hku.hk; lawrence.chennan@gmail.com; yixicai@connect.hku.hk; xuweii@hku.hk; fuzhang@hku.hk).

This article has supplementary material provided by the authors and color versions of one or more figures available at https://doi.org/10.1109/TMECH.2022.3153587.

Digital Object Identifier 10.1109/TMECH.2022.3153587

of control authority, but with less moment of inertia. Similar to tandem tilt-rotor, Özdoğan and Leblebicioğlu [22] proposed an efficient heavy-lift helicopter consisting of two large propellers providing efficient thrust and two small tilting rotors to control the attitude.

The one thing that all the bi-copters mentioned above have in common is that they all rely on external actuators to provide pitch, roll, and yaw control authority. The servo motors used on tandem rotor configuration always require high torque and quick response, and this will narrow the choice of servo motors options down to relative heavy metal gears, which, in turn, adds on weight and lowers its efficiency. Besides, the backlash inside the servo motor gearbox also might increase the system's nonlinearity. Moreover, the control bandwidth is restricted by the mechanical nature of servo motors. As shown in Li *et al.* [19], the roll dynamics of a servo-driven tandem rotor bi-copter is the nonminimum phase, which fundamentally limits the attainable controller bandwidth [23].

To reduce the number of actuators, increase reliability, reduce cost, and weight for micro air vehicle (MAV), Paulos and Yim [24] first proposed a dual rolls swashplate-less mechanism. By driving the brushless motor through position-dependent signal, pitching and rolling torque can be generated without requiring either additional servo motors or complex linkages like traditional swashplate. The swashplate-less mechanism was applied to a 227-g coaxial helicopter MAV [25], and its performance is validated by closed-loop trajectory tracking. The subsequent work [26] further introduced flap hinges to the swashplate-less mechanism. The detailed kinetics and dynamic models, including hinge losses, are discussed. The author stated that this skewed lag-pitch hinge enables a smoother harmonic flapping response and reduced vibrations. According to Paulos and Yim [27], the swashplate-less mechanism is highly scalable. The cyclic blade pitch control has been demonstrated in rotors from 10 cm to 1 m, at operating speeds ranging from 300 to 9000 r/min. [28] merged two teetering hinges into one. By adopting such a new mechanism, the coaxial helicopter prototype can emulate a fully actuated MAV.

Toward the goal of increasing the control bandwidth, mechanical reliability, efficiency, and mitigating the nonminimum phase behavior brought by servo motors, we adopted a cyclic blade pitch control technique with similar working principles as [28] and combined the benefit of the swashplate-less mechanism and the high efficiency of the bi-copter configuration. As found in the original work [24], this swashplate-less mechanism has a dead-zone nonlinearity in control response at low-drive amplitude ascribed to sliding friction. To avoid this issue, we improve the swashplate-less mechanism by using ball bearings and thrust bearings in the hinges. As a result, our approach is a servo-less bi-copter UAV, as shown in Fig. 1. Magnetic encoders are placed beneath the center of the brushless motor rotating shaft, providing rotor angle feedback to the flight controller. The motor torque is modulated depending on the angle feedback to excite a lead–lag motion of the swashplate-less mechanism and make a once-per-revolution variation in blade pitch. Instead of depending on servo motors to produce torque in roll (same tilting direction of the two rotor disks) and yaw (different tilting direction of the disks), this bi-copter UAV achieves improved attitude control performance with only passive hinges.

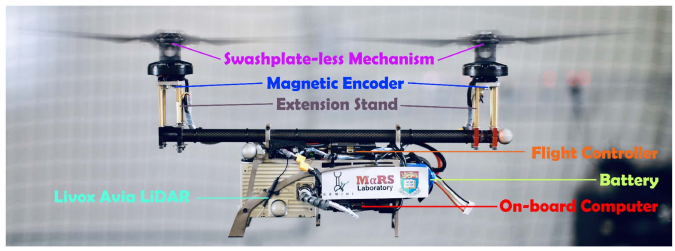

Fig. 2. Gemini II mechanical design detail and avionics.

In this article, we mainly focus on overall system architecture, implementation, controller design, power consumption, and the flight performance of the bi-copter. Our contributions are as follows: 1) We improve the swashplate-less mechanism and eliminate the dead zone nonlinearity in control response at low-drive amplitudes compared to [24]. 2) Based on this swashplate-less mechanism, we develop a novel servoless bi-copter configuration and detailed dynamics model. 3) We design an effective cascaded proportional-integral-derivative (PID) controller and control allocation scheme and implement them all on off-the-shelf electronics without using any custom motor controllers as in prior works [24]–[28]. 4) We demonstrate the validity and flight performance by conducting a series of flight tests, including power consumption test, poking disturbance test, gust wind disturbance test, step response test, and agile trajectory tracking.

The rest of this article is organized as follows. Section II elucidates the system architecture and mechanical design details, the vibration issue caused by the propulsion system, and other factors that affect the system stability. Section III explicates the system models, controller, and mixers logic that is behind the Gemini II. Multiple flight experiment results and disturbance tests are interpreted in Section IV. Finally, Section VI concludes this article.

II. System Architecture and Mechanical Design

Fig. 2 shows the main components of our developed bi-copter UAV, Gemini II. When compared to our previous tandem rotor bi-copter, Gemini [12], the most apparent difference is the propulsion system. Instead of using servo motors to tilt the propeller disk to gain all four degrees of freedom control authorities, the cyclic blade pitch control mechanism is utilized. As detailed in Section II-C, this mechanism requires no extra actuator (e.g., servo motor) to tilt the rotor disk. As a consequence, the Gemini II has only two actuators, whose speeds are controlled by a 45-A two-in-one electrical speed controller (ESC).

Extension stands are placed beneath the brushless motors to increase the distance from the propeller to the center of mass (COM), and therefore increase the torque on the roll or yaw direction when the same amount of lateral force is generated (see Section III-B). Since hinges are connecting the blade and motors, due to gravity, propeller blades tend to flap down

when the motor stops spinning. The extension stands also serve the function of protecting propellers from hitting the drone's body.

A. Fuselage

The fuselage is made with a 3D-printed aluminum body. Two propulsion units are attached at the two ends of the 41 cm long carbon fiber rod. To minimize the differential thrust between the front and back rotor, we make the fuselage movable on the carbon fiber rod. By adjusting the fuselage position, the COM can be manually shifted to the center of the aircraft. Without balancing the COM, the propulsion unit will be forced to generate pitch torque while hovering. In the worst-case scenario, one side of the propulsion unit will be close to saturation, leaving little room for sinusoidal manipulation, and making the aircraft lose control ability over yaw and roll.

B. Avionics

In our bi-copter prototype, PX4 flight controller hardware is used, but the key controller, including the mixer, is customized as detailed in Section III-B. The onboard computer is an ARM-based single-board computer, and it serves as a relay that transmits the position data from the Vicon motion capture system to the flight controller. In the future, with the onboard Livox Avia LiDAR providing a 3-D point cloud, real-time SLAM algorithms can be performed on the onboard computer, yielding position feedback without depending on an external motion capture system. The Fuli 5000-mAh 5S HV battery can be charged up to 4.35 V per cell on the daily basis. It provides power for all the onboard electronics, and the actual flight time lasts 22 min.

C. Cyclic Blade Pitch Control Mechanism

Benefiting from the cyclic blade pitch control mechanism proposed in [26], the thrust generated by the propulsion system is able to change direction with the addition of only three passive hinges. Fig. 3 shows a complete set of cyclic blade pitch control mechanisms, which consists of a set of swashplate-less mechanisms (shown in the upper side of Fig. 3), a pair of propellers blades, a brushless dc motor, and a magnetic encoder board placed at the bottom of the rotor (shown in the lower right corner of Fig. 3). The two blades are tightly mounted on their respective side hubs, which are then connected to a teetering hub through two passive lag-pitch hinges. A third passive hinge, the teetering hinge, is further used to connect the teetering hub to the central hub which is firmly attached to the rotor. As a result, the two blades and the teetering hub can freely rotate about their respective hinges, and the whole mechanism is driven by the motor.

1) Working Principle: Fig. 4 illustrates the working principle of the cyclic blade pitch control mechanism. To ease the explanation, a motor frame $\mathcal{M}$ with its z-axis along the rotation axis of the motor is introduced. When the motor accelerates at angular location γ, the two blades [colored in green in Fig. 4(a)] will not accelerate immediately due to blade inertia, causing a lag from its supposed positions (colored in blue). As a consequence, the

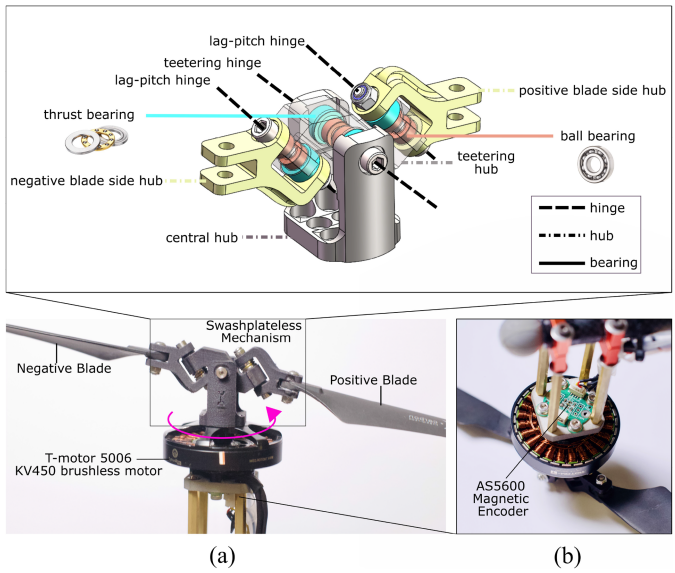

Fig. 3. Cyclic pitch control mechanism with partial closeup. (a) Cyclic pitch control mechanism (b) Magnetic encoder closeup.

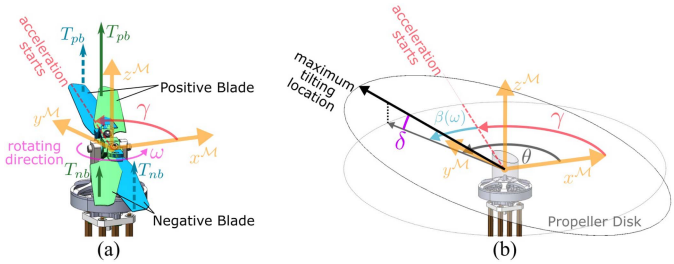

Fig. 4. Blade dynamic reaction on the counterclockwise spinning motor. (a) Lagging behavior of the two blades. (b) Tilting of the propeller disk.

two blades will further rotate around their respective lag-pitch hinges. Because of the special lag-pitch hinge arrangement, the rotation of the positive blade will lead to an increased pitch angle (hence larger thrust T_{pb}) while the rotation of the negative blade will lead to a decreased pitch angle (hence smaller thrust T_{nb}). The thrust difference will then cause the two blades (hence the propeller disk) to rotate around the teetering hinge. The tilting of the propeller disk further causes a tilting of the total thrust $T = T_{pb} + T_{nb}$.

In practice, to prevent the possible vibration excited by a sudden jump in the rotor acceleration, a sinusoidal rotor acceleration profile is typically employed [26]. More specifically, the motor throttle command U is designed as

$$U = C + A\sin(\alpha - \gamma) \tag{1}$$

where C is the nominal throttle (e.g., at hovering) that produces the average motor speed ω and total thrust T, A is the amplitude, α is the current angular location of rotor measured by the magnetic encoder, and γ is the angular location where the motor starts to accelerate. In [26], it is shown that the maximal angle the two blades rotate around the teetering hinge (i.e., the disk tilting angle) δ [see Fig. 4(b)] is approximately proportional to

A by K_a, i.e.,

$$\delta = K_a A \tag{2}$$

while the maximal tilting location of the blades (referred from the x-axis of the motor frame $\mathcal{M}$) is

$$\theta = \gamma + \beta(\omega) \tag{3}$$

where β is a lag angle of the blades' maximal tilting location θ relative to the γ due to the tilting dynamic response of the blades. Typically, β depends on the average motor speed ω and can be calibrated in experiments.

Changing γ in the motor command (1) will change the maximum tilting location of the propeller disk, thus vectoring the thrust. In practice, we could restrict the range of γ such that θ is within $[0, \pi]$ and flip the sign of A [hence δ by (2)] to attain a negative tilting of the disk. As a result, the motor thrust vector expressed in the motor frame $\mathcal{M}$ is

$$\boldsymbol{F}^{\mathcal{M}} = \boldsymbol{R}(\theta \cdot \boldsymbol{e}_3)\boldsymbol{R}(\delta \cdot (-\boldsymbol{e}_2)) \cdot (T \cdot \boldsymbol{e}_3) \tag{4}$$

where $\boldsymbol{R}(\boldsymbol{a})$ denotes the rotation matrix about an axis-angle $\boldsymbol{a} \in \mathbb{R}^3$ and $\boldsymbol{e}_i \in \mathbb{R}^3$ has its ith element equal to one and other elements equal to zeroes.

2) Implementation Details: Compared to the design from [28], we employed an M3 half-thread hex bolt that was customized with CNC machines instead of using thin steel wire as hinges. Due to the high frequency of rotating caused by the much larger aircraft weight, the plastic hubs in [28] could easily be heated up to their melting point by sliding friction, resulting in a larger gap between the hinges and the hub, causing vibration in the long run. With precisely manufactured CNC bolts and commercial ball bearing, the friction between hinges and hubs is minimized. Moreover, with the addition of bearings, the moment magnitude means response no longer has a dead-zone nonlinearity in control response at low-drive amplitudes ascribed to sliding friction, and becomes highly linear (see test results in Fig. 10) when compared to previous works [24]. Each hinge is clasped by two ball bearings on both ends, ensuring the central hub has a firmer grip over the lag-pitch hinges when counteracting with the lateral component of the centrifugal force while the mechanism is rotating. Two thrust bearings on the teetering hinge are aiming to transfer the sliding friction between the central hub and the teetering hub into rolling friction, which is significantly smaller than the former. On each side of the lag-pitch hinge, only one thrust bearing is placed between the side hub and the central hub. The reason behind this is that once the mechanism starts to spin, the lateral component of the centrifugal force will push the side hubs side-way, increasing only the pressure on the contacting surface where the thrust bearing is currently placed. Since manufacturing errors are unavoidable, an even tightness between the lag-pitch hinge is critical to dynamic response excited by modulated shaft torque from the driving motor. Uneven pressures on lag-pitch hinge thrust bearings will result in different pitch angles on two sides of the propeller, generating a high-frequency vibration at the same frequency as the motor rotation. In practice, adjusting the nylon-insert lock nut on the lag-pitch hinge so that it is loose enough to allow the side hubs to rotate freely will avoid such an issue. It is also worthwhile to point out that each pair of the thrust bearing and ball bearing could be replaced with a single tapered roller bearing, but miniature thrust bearing and ball bearing are easily available off-the-shelf components while mini single tapered roller bearing is not. Out of practical and cost concerns, the current design is chosen. For the propeller, T-MOTOR MF1302 propeller blades are made of lightweight polymer, which minimizes the rotational inertia and the torque needed for the motor to frequently change its acceleration. The T-MOTOR MN5006 KV450 brushless motor has both relatively low motor velocity constant (KV) value and resistance, which enables a slower rotational speed and generates less heat when generating high rotational torque. The magnetic encoder unit is a customized PCB board with AS5600 placed at the center, as shown in Fig. 3(b). The AS5600 magnetic encoder interprets rotor position with a resolution of $2\pi/4096$ by an update frequency at 920 Hz. Note that the experimental maximum rotation speed is about 5000 r/min, which equals 83 Hz. The ESC is running with the OneShot125 protocol, so the motor command is updating at 4 kHz, and at least 48 motor commands can be sent out during each rotation cycle.

III. System Modeling and Control

A. Modeling

1) Coordinate Systems: Fig. 5 shows the definition of all four right-handed coordinate frames of Gemini II. The North-East-Down (NED) inertia frame $\mathcal{I}$ is a world-fixed frame whose origin coincides with the origin of the Vicon motion capture system and the direction of the z-axis is the same as the gravity vector. The Forward-Right-Down (FRD) body frame $\mathcal{B}$ is a motion frame whose origin coincides with the COM of the Gemini II. Two frames represented as $\mathcal{M}_1$ and $\mathcal{M}_2$, are attached to motor rotors, and the origins of both are at the center, at two teetering hinges, respectively. Motor 1 (the front motor) rotates counterclockwise and motor 2 (the back motor) rotates clockwise from the top view. The motor rotor angle α_1, α_2, and the disk tilting angle δ_1, δ_2 follow the same definition as in Section II-C1.

2) Forces and Moments: To control the four degrees of freedom of the Gemini II (i.e., position and yaw), it is sufficient that the propeller disk is only tilted along the y-axis of the body frame (i.e., $\theta = \pi$). Hence, the γ in the motor command (1) is calculated as

$$\gamma = \pi - \beta(\omega) \tag{5}$$

and the resultant propeller thrust from (4) is

$$F_y^{\mathcal{B}} = F_x^{\mathcal{M}} = T \sin\delta \tag{6a}$$

$$F_z^{\mathcal{B}} = F_z^{\mathcal{M}} = T \cos\delta \tag{6b}$$

$$F_x^{\mathcal{B}} = F_y^{\mathcal{M}} = 0. \tag{6c}$$

Because the Gemini II has two motors, a subscript $i, i = 1, 2$ is adopted to $F_y^{\mathcal{B}}$ and $F_z^{\mathcal{B}}$ for representing which motor the thrust is generated from. According to the geometry of the mechanical

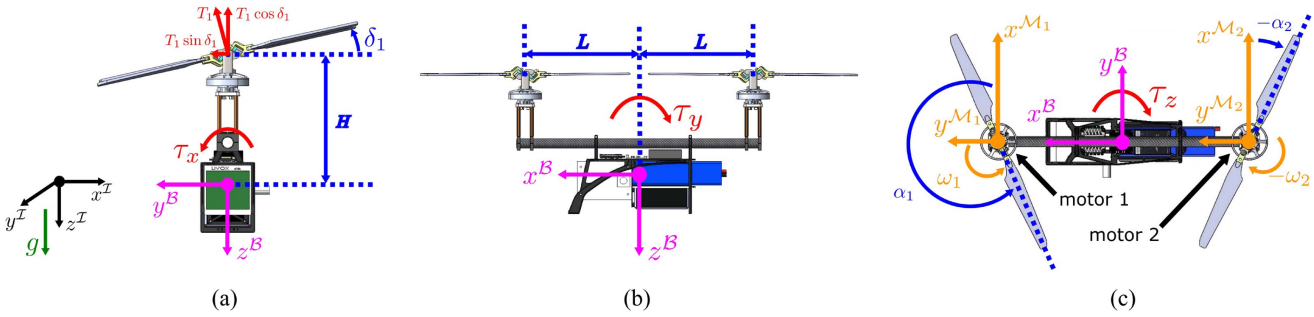

Fig. 5. Definition of coordinate frames. (a) Front view. (b) Side view. (c) Top view.

structure of Gemini II (see Fig. 5), we can obtain

$$\begin{bmatrix} f^{\mathcal{B}}_{T,z} \\ \tau^{\mathcal{B}}_x \\ \tau^{\mathcal{B}}_y \\ \tau^{\mathcal{B}}_z \end{bmatrix} = \begin{bmatrix} 1 & 1 & 0 & 0 \\ 0 & 0 & H & H \\ L & -L & 0 & 0 \\ 0 & 0 & L & -L \end{bmatrix} \begin{bmatrix} F^{\mathcal{B}}_{z,1} \\ F^{\mathcal{B}}_{z,2} \\ F^{\mathcal{B}}_{y,1} \\ F^{\mathcal{B}}_{y,2} \end{bmatrix} \tag{7}$$

where H is the body z-axis direction distance from the teetering hinge of swashplate-less structure to the COM, L is the body x-axis direction distance from the motor-mounted position to the COM. $f^{\mathcal{B}}_{T,z}$ is the total thrust in the body z-axis. $\tau^{\mathcal{B}}_j, j = x, y, z$ are three moments along the body x-, y-, and z-axes, respectively.

3) Dynamics: The dynamics of the Gemini II can be represented in a standard rigid motion with both translation and rotation

$$\begin{bmatrix} m\boldsymbol{I} & 0 \\ 0 & \boldsymbol{J}^{\mathcal{B}} \end{bmatrix} \begin{bmatrix} \dot{\boldsymbol{v}}^{\mathcal{I}} \\ \dot{\boldsymbol{\omega}}^{\mathcal{B}} \end{bmatrix} + \begin{bmatrix} 0 \\ \widehat{\boldsymbol{\omega}}^{\mathcal{B}} \boldsymbol{J}^{\mathcal{B}} \boldsymbol{\omega}^{\mathcal{B}} \end{bmatrix} = \begin{bmatrix} \boldsymbol{f}^{\mathcal{I}}_g \\ 0 \end{bmatrix} + \begin{bmatrix} \boldsymbol{R} \boldsymbol{f}^{\mathcal{B}}_T \\ \boldsymbol{\tau}^{\mathcal{B}} \end{bmatrix} \tag{8a}$$

$$\boldsymbol{R} = \boldsymbol{R}_z(\psi)\boldsymbol{R}_y(\lambda)\boldsymbol{R}_x(\varphi) \tag{8b}$$

where m, $\boldsymbol{I}$, and $\boldsymbol{J}^{\mathcal{B}}$ stand for the mass, the identity matrix in $\mathbb{R}^{3\times3}$, and the inertia matrix in the body frame, respectively. $\boldsymbol{\omega}^{\mathcal{B}}$ is the angular velocity vector represented in the body frame while $\widehat{\boldsymbol{\omega}}^{\mathcal{B}}$ is the skew-symmetric cross-product matrix of $\boldsymbol{\omega}^{\mathcal{B}}$, $\boldsymbol{v}^{\mathcal{I}}$ is the velocity vector represented in the inertial frame. $\boldsymbol{f}^{\mathcal{I}}_g = [0\ 0\ mg]^T$ stands for the gravity in the inertial frame, and the thrust vector in body frame is $\boldsymbol{f}^{\mathcal{B}}_T = [0\ 0\ f^{\mathcal{B}}_{T,z}]^T$. $\boldsymbol{\tau}^{\mathcal{B}} = [\tau^{\mathcal{B}}_x\ \tau^{\mathcal{B}}_y\ \tau^{\mathcal{B}}_z]^T$ is the moment vector. $\boldsymbol{R}$ is the rotation matrix from the inertial frame to the body frame following the $z-y-x$ Tait–Bryan order, where ψ, λ, and φ stand for the Euler angle yaw, pitch, and roll, respectively.

It should be noted that three simplifications are adopted in the above modeling process. 1) The propeller torques are ignored in $\boldsymbol{\tau}^{\mathcal{B}}$ as it is usually small when compared to the torques induced by thrust. 2) The gyroscopic torque, which comes from the direction change of the angular momentum of the propeller when the rotating plane of propeller tilts by the swashplate-less structure, is also not modeled in $\boldsymbol{\tau}^{\mathcal{B}}$ because the inertia of rotor and propeller is quite small when compared to the inertia of the whole aircraft. Also, this torque only occurs in the transient response of roll and yaw rotation and is zero when the roll and yaw angle converge to the desired values. 3) In the calculation for the force vector $\boldsymbol{f}^{\mathcal{B}}_T$, due to the tilt angle of the rotating plane of the propeller, the thrust projected to the xy plane of the body frame is neglected. Similar to the situation of gyroscopic torque, this force is only produced in the transient response of roll rotation and becomes zero when it converges to the desired value. The neglected torque and force can simplify the dynamic model; however, it will lead to some dynamics remaining unmodeled. In this article, we focus on designing the baseline controller that aims to stabilize the overall system. For this purpose, the three simplifications are valid, as shown in the actual experiments.

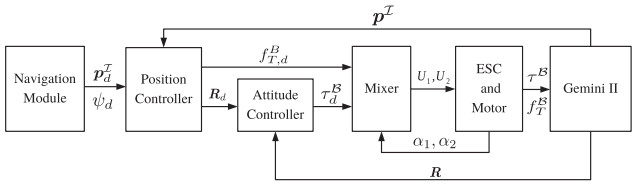

Fig. 6. Control system structure.

B. Control

1) Control System Structure: The whole control structure of the Gemini II is shown in Fig. 6. The navigation module produces the desired position $\boldsymbol{p}_d$ and yaw angle ψ_d for the position controller to track. The position controller will generate the desired attitude $\boldsymbol{R}_d$ and body z-axis force T_d. The attitude controller will calculate the desired moment $\boldsymbol{\tau}^{\mathcal{B}}_d$ based on the desired attitude. Finally, according to the T_d, $\boldsymbol{\tau}^{\mathcal{B}}_d$, and real-time angular position of the motor rotor, the mixer will calculate the motor throttles that will be sent to the ESC for controlling the motors to drive propellers.

2) Position Controller: The position controller of the Gemini II is a cascaded controller with proportional gain K^p_p and an inner velocity loop. The desired velocity $\boldsymbol{v}^{\mathcal{I}}_d$ is calculated as follows:

$$\boldsymbol{v}^{\mathcal{I}}_d = K^p_p \cdot \boldsymbol{p}^{\mathcal{I}}_e = K^p_p \cdot \left(\boldsymbol{p}^{\mathcal{I}}_d - \boldsymbol{p}^{\mathcal{I}}\right) \tag{9}$$

where $\boldsymbol{p}^{\mathcal{I}}_e$, $\boldsymbol{p}^{\mathcal{I}}_d$, and $\boldsymbol{p}^{\mathcal{I}}$ are the position error, desired position, and current position in the inertia frame, respectively.

The velocity loop is a full PID controller and its output is the desired acceleration $\boldsymbol{a}^{\mathcal{I}}_d$ that is calculated by the desired velocity and current velocity as

$$\boldsymbol{v}^{\mathcal{I}}_e = \boldsymbol{v}^{\mathcal{I}}_d - \boldsymbol{v}^{\mathcal{I}} \tag{10a}$$

$$\boldsymbol{a}^{\mathcal{I}}_d = K^v_p \cdot \boldsymbol{v}^{\mathcal{I}}_e + K^v_i \cdot \int \boldsymbol{v}^{\mathcal{I}}_e dt + K^v_d \cdot \dot{\boldsymbol{v}}^{\mathcal{I}}_e \tag{10b}$$

where $\boldsymbol{v}_e^{\mathcal{I}}$ and $\boldsymbol{v}^{\mathcal{I}}$ are the velocity error and current velocity, respectively; K_p^v, K_i^v, and K_d^v are the gains of PID actions in the velocity loop.

When the desired acceleration is obtained, the desired attitude $\boldsymbol{R}_d$ and force $\boldsymbol{f}_{T,d}^{\mathcal{B}} = [0\ 0\ f_{T,z,d}^{\mathcal{B}}]^T$ can be solved from the below equation following the method in [29]

$$m\boldsymbol{a}_d^{\mathcal{I}} = \boldsymbol{f}_g^{\mathcal{I}} + \boldsymbol{R}_d \boldsymbol{f}_{T,d}^{\mathcal{B}}. \tag{11}$$

It should be noted that a rotation around the body z-axis does not affect the force direction, hence the yaw angle can be freely specified. Once the desired yaw angle is specified, the whole desired attitude $\boldsymbol{R}_d$ can be uniquely determined and will be used as the input of the attitude controller.

3) Attitude Controller: The attitude controller is also cascaded. The outer loop (i.e., angular loop) is a proportional controller to track the desired attitude $\boldsymbol{R}_d$. The quaternion ($\boldsymbol{q} = [w, \boldsymbol{r}^T]^T$) is used to represent the attitude, where w and $\boldsymbol{r}$ denote the scalar and vector part of the quaternion, respectively. With the quaternion representation, the attitude error $\boldsymbol{q}_e$ and desired angular velocity $\boldsymbol{\omega}_d^{\mathcal{B}}$ are calculated based on the "quaternion linear" method in [30]

$$\boldsymbol{q}_e = \boldsymbol{q}^* \otimes \boldsymbol{q}_d = \begin{bmatrix} w_e & \boldsymbol{r}_e^T \end{bmatrix}^T \tag{12a}$$

$$\eta = 2 \cdot \arctan2\left(\|\boldsymbol{r}_e\|, w_e\right) \tag{12b}$$

$$\boldsymbol{\omega}_d^{\mathcal{B}} = K_p^a \cdot \boldsymbol{\xi}_e^{\mathcal{B}} = K_p^a \cdot \operatorname{sign}(w_e) \cdot \frac{\eta}{\sin(\frac{\eta}{2})} \boldsymbol{r}_e \tag{12c}$$

where $\boldsymbol{q}_d$ and $\boldsymbol{q}$ are the desired and actual attitude, operators $*$ and $\otimes$ denote the conjugate and multiplication operation of quaternion, respectively, and K_p^a is a proportional gain from attitude error $\boldsymbol{\xi}_e^{\mathcal{B}}$ to desired angular velocity $\boldsymbol{\omega}_d^{\mathcal{B}}$.

The inner loop (i.e., angular velocity loop) is a PID controller used to track the desired angular velocity $\boldsymbol{\omega}_d^{\mathcal{B}}$, which can be represented as

$$\boldsymbol{\omega}_e^{\mathcal{B}} = \boldsymbol{\omega}_d^{\mathcal{B}} - \boldsymbol{\omega}^{\mathcal{B}} \tag{13a}$$

$$\boldsymbol{\tau}_d^{\mathcal{B}} = K_p^w \cdot \boldsymbol{\omega}_e^{\mathcal{B}} + K_i^w \cdot \int \boldsymbol{\omega}_e^{\mathcal{B}} dt + K_d^w \cdot \dot{\boldsymbol{\omega}}_e^{\mathcal{B}} \tag{13b}$$

where $\boldsymbol{\omega}_e^{\mathcal{B}}$ and $\boldsymbol{\omega}^{\mathcal{B}}$ are angular velocity error and current angular velocity, respectively. K_p^w, K_i^w, and K_d^w are the gains of PID terms in the angular velocity loop. The output of the inner loop is the desired moment $\boldsymbol{\tau}_d^{\mathcal{B}} = [\tau_{x,d}\ \tau_{y,d}\ \tau_{z,d}]^T$.

4) Mixer: The mixer is used to calculate the motor throttles (U_1, U_2) that produces the desired moment $\boldsymbol{\tau}_d^{\mathcal{B}}$ and force $f_{T,z,d}^{\mathcal{B}}$. Combining (6) and (7), because the tilt angles of propeller disks are small during normal operation, the result can be simplified as

$$\begin{bmatrix} f_{T,z}^{\mathcal{B}} \\ \tau_x^{\mathcal{B}} \\ \tau_y^{\mathcal{B}} \\ \tau_z^{\mathcal{B}} \end{bmatrix} = \begin{bmatrix} 1 & 1 & 0 & 0 \\ 0 & 0 & H & H \\ L & -L & 0 & 0 \\ 0 & 0 & L & -L \end{bmatrix} \begin{bmatrix} T_1 \\ T_2 \\ T_1\delta_1 \\ T_2\delta_2 \end{bmatrix} \tag{14}$$

where T_i and δ_i are the motor thrust and tilting angle of the propeller disk of motor $i, i = 1, 2$, respectively.

Given the desired moment vector $\boldsymbol{\tau}_d^{\mathcal{B}} = [\tau_{x,d}^{\mathcal{B}}\ \tau_{y,d}^{\mathcal{B}}\ \tau_{z,d}^{\mathcal{B}}]^T$ and force $f_{T,z,d}^{\mathcal{B}}$, the desired body z-axis motor thrust ($T_{1,d}$, $T_{2,d}$) and body y-axis force ($T_{1,d}\delta_{1,d}$, $T_{2,d}\delta_{2,d}$) can be solved from (14) as follows:

$$\begin{bmatrix} T_{1,d} \\ T_{2,d} \\ T_{1,d}\delta_{1,d} \\ T_{2,d}\delta_{2,d} \end{bmatrix} = \begin{bmatrix} \frac{1}{2} & 0 & \frac{1}{2L} & 0 \\ \frac{1}{2} & 0 & \frac{-1}{2L} & 0 \\ 0 & \frac{1}{2H} & 0 & \frac{1}{2L} \\ 0 & \frac{1}{2H} & 0 & \frac{-1}{2L} \end{bmatrix} \begin{bmatrix} f_{T,z,d}^{\mathcal{B}} \\ \tau_{x,d}^{\mathcal{B}} \\ \tau_{y,d}^{\mathcal{B}} \\ \tau_{z,d}^{\mathcal{B}} \end{bmatrix} \tag{15}$$

where $T_{1,d}$ and $T_{2,d}$ are the desired thrust of the front and rear motor, $\delta_{1,d}$ and $\delta_{2,d}$ are the desired tilt angles of the front and rear propeller disks. The motor throttles (U_1, U_2) can be calculated as

$$\begin{bmatrix} U_1 \\ U_2 \end{bmatrix} = \begin{bmatrix} K_t & 0 \\ 0 & K_t \\ \sin(\alpha_1 - \gamma_1) & 0 \\ 0 & \sin(\alpha_2 - \gamma_2) \end{bmatrix}^T \begin{bmatrix} T_{1,d} \\ T_{2,d} \\ \frac{\delta_{1,d}}{K_a} \\ \frac{\delta_{2,d}}{K_a} \end{bmatrix} \tag{16}$$

where K_t and K_a are positive proportion coefficients from propeller thrust to the corresponding motor throttle, and from sinusoidal amplitude to tilting angle of propeller disk, respectively. $\alpha_i, i = 1, 2$ is the angular location of motor i measured by the magnet encoder, $\gamma_i = \pi - \beta_i(\omega), i = 1, 2$.

According to (15) and (16), the relation between motor throttles and desired moments and force can be finally derived as

$$U_1 = C_1 + A_1 \sin(\alpha_1 - \gamma_1) \tag{17a}$$

$$U_2 = C_2 + A_2 \sin(\alpha_2 - \gamma_2) \tag{17b}$$

$$C_1 = \frac{K_t}{2} f_{T,z,d}^{\mathcal{B}} + \frac{K_t}{2L} \tau_{y,d}^{\mathcal{B}}, A_1 = \frac{1}{K_a T_{1,d}} \left(\frac{\tau_{x,d}^{\mathcal{B}}}{2H} + \frac{\tau_{z,d}^{\mathcal{B}}}{2L} \right) \tag{17c}$$

$$C_2 = \frac{K_t}{2} f_{T,z,d}^{\mathcal{B}} - \frac{K_t}{2L} \tau_{y,d}^{\mathcal{B}}, A_2 = \frac{1}{K_a T_{2,d}} \left(\frac{\tau_{x,d}^{\mathcal{B}}}{2H} - \frac{\tau_{z,d}^{\mathcal{B}}}{2L} \right). \tag{17d}$$

Fig. 7. Actuator evaluation setup.

IV. Experiment Results

To verify the feasibility and performance of the servoless bi-copter design, we first test the actuators on a test bench, as shown in Fig. 7, then compared the agility among Gemini II, quadcopter, and our previous servo bi-copter, Gemini mini [12]. Using the well-tuned parameters, we identified the external force disturbance rejection model. Then, we conduct two disturbance

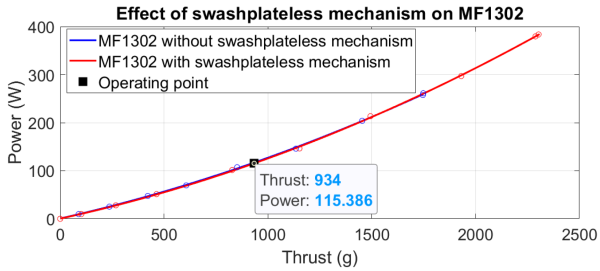

Fig. 8. Effect of the swashplate-less mechanism on the power efficiency.

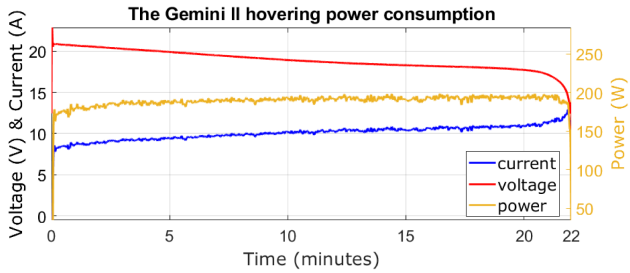

Fig. 9. Gemini II hovering power consumption.

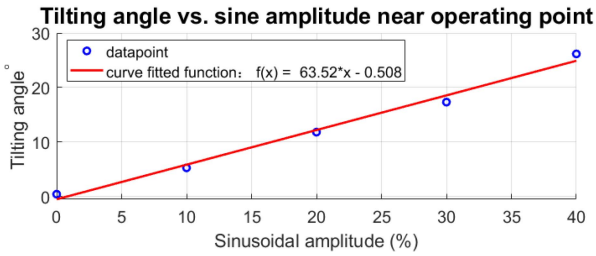

Fig. 10. Tilting angle versus sinusoidal amplitude near operating point.

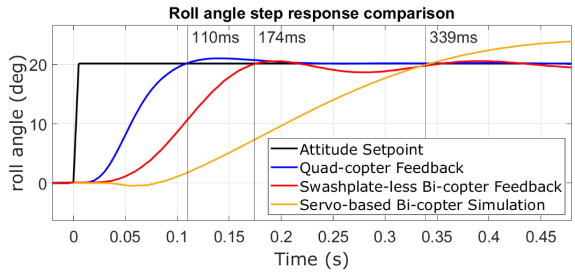

Fig. 11. Roll angle step response comparison.

tests, along with a trajectory tracking experiment on the complete UAV, Gemini II. Videos showing the UAV performance in these tests are available in the supplementary material.

A. Actuators Evaluation

1) Power Consumption: We first study the effect of the swashplate-less mechanism on propeller power consumption. Fig. 8 shows the power comparison of the original 13.4-in propeller MF1302 and its modification with the swashplate-less mechanism, which is 1-in wider due to bearing and hinges, at different thrust. As can be seen, the power consumption results are very close with and without the swashplate-less mechanism. By the prediction of the ideal disk loading theory, the increase in propeller size should boost efficiency up by 7%, but the absence of such behavior indicates the swashplate-less mechanism lowers the efficiency by 7% mainly because the optimized design of the propeller blade is affected by the slight change of the angle of attack and the increased diameter. Moreover, due to the slightly increased propeller size, the variant with a swashplate-less mechanism obtains a larger maximal thrust. Fig. 8 also shows the operating point of the propeller at hovering. The operating point is near 50% PWM, reserving a safe margin for the sinusoidal drive command and avoiding saturation. Fig. 9 shows the power consumption of the Gemini II during the flight endurance test. The average power consumption during hovering is 193 W, which indicates each propulsion system consumes 96.5 W of power. The error between the measured power consumption during flight and the prediction (see Fig. 8) might be due to the imprecision of the onboard power monitoring module. With the 5S 5000 mAh battery onboard, the actual test lasted for 22 min and the landing automatically initiated after the battery voltage is observed below 16.5 V. The Gemini II weighs 1869 g (including a 600-g LiDAR payload), making its hovering efficiency 9.68 g/W.

2) Sinusoidal Throttle Command: To verify the assumption we made earlier in Section II-C1 that the relation between δ and A is proportional, we fixed the voltage to 21 V and conducted a sinusoidal amplitude sweeping command test when the propeller is rotating at the hovering speed. As shown in Fig. 10, the relation is highly linear with no clear sign of dead-zone, and (2) can be curve-fitted into the function shown in the legend. In practice, we limit the sinusoidal amplitude below $A_{\max} = 26\%$ to ensure the side hubs do not collide with the teetering hub, and the motor does not overheat. Similar to [25], we also calibrated the relation between β and ω, and compensated the angle lag in the controller.

3) Agility Comparison: To demonstrate the agility of the UAV with the swashplate-less mechanism, step response tests on roll attitude were conducted on Gemini II, our previous servo-based bi-copter, Gemini mini [12], and a quadcopter, all with the same width and weight. The tests on Gemini II and the quadcopter are conducted on actual UAVs, and the test on Gemini mini is performed on a high-fidelity model identified by a sweep sine excitation [19]. Gemini II and the quadcopter UAV are controlled by well-tuned PID controllers and the Gemini mini is controlled by a high-gain optimal controller designed by H-infinity synthesis [19]. The three UAVs were initially hovering without position feedback; at time zero, 20-degree roll angle attitude commands were given to the UAV. As shown in Fig. 11, the quadcopter quickly reached the attitude target at 110 ms, while Gemini II has a larger rise time of 174 ms. In contrast, the servo-based bi-copter, Gemini mini, despite its high-gain controller, has a rise time of 339 ms. When comparing the actuator time constant T of the two bi-copters, Gemini II has a T of 28.5 ms, while Gemini mini has a T of 33.2 ms with an additional 30-ms pure time-delay (see (6) of [19]). We also

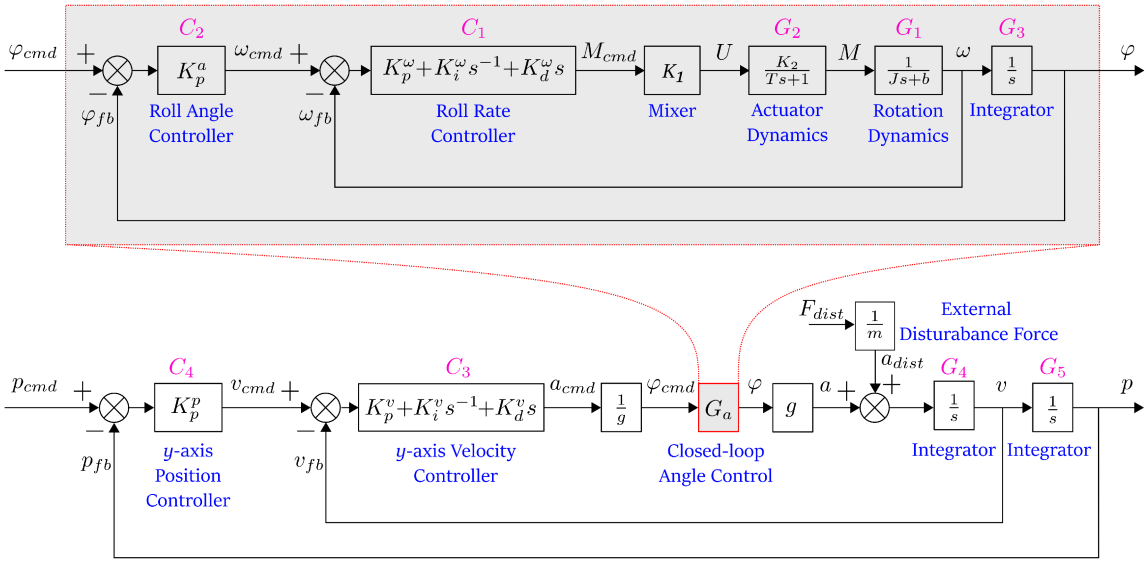

Fig. 12. y-Axis position control system structure of the Gemini II.

notice that the servo-based bi-copter exposes a clear nonminimum phase phenomenon where the response goes first toward the opposite direction of the command. This phenomenon is much mitigated and almost negligible in Gemini II. The excelsior actuator response and the vanished behavior of the nonminimum phase nature of the Gemini II results in a great improvement in agility when compared to servo bi-copters, yet it is still outmatched by quadcopters at a cost of 55% higher average hovering power consumption.

B. Model Identification and Disturbance Rejection Analysis

In this section, we perform disturbance analysis of the overall aircraft, especially along the roll direction (or y-axis) which differs the most from the standard quadcopter. Fig. 12 shows the diagrams of y-axis position control. The upper diagram inside of the red box represents the closed-loop roll angle control system and the lower diagram indicates the complete closed-loop y-axis position control system. The closed-loop transfer function of the roll rate loop, roll angle loop, y-axis velocity loop, and y-axis position loop are G_r, G_a, G_v, and G_p, respectively. They can be calculated as

$$G_r = \frac{\omega_{\text{fb}}(s)}{\omega_{\text{cmd}}(s)} = \frac{K_1 C_1 G_1 G_2}{1 + K_1 C_1 G_1 G_2} \tag{18}$$

$$G_a = \frac{\varphi_{\text{fb}}(s)}{\varphi_{\text{cmd}}(s)} = \frac{C_2 G_r G_3}{1 + C_2 G_r G_3} \tag{19}$$

$$G_v = \frac{v_{\text{fb}}(s)}{v_{\text{cmd}}(s)} = \frac{C_3 G_a G_4}{1 + C_3 G_a G_4} \tag{20}$$

$$G_p = \frac{p_{\text{fb}}(s)}{p_{\text{cmd}}(s)} = \frac{C_4 G_v G_5}{1 + C_4 G_v G_5} = \frac{C_3 C_4 G_a G_4 G_5}{1 + C_3 G_a G_4 + C_3 C_4 G_a G_4 G_5}. \tag{21}$$

TABLE I
GEMINI II y-AXIS CONTROL PARAMETERS

Controller	Parameters		
Roll angle (C_2)		$K_p^a = 13$	
y-axis Velocity (C_3)	$K_p^v = 1.8$	$K_i^v = 0.4$	$K_d^v = 0.2$
y-axis Position (C_4)		$K_p^p = 0.95$	

The transfer function from the external force disturbance F_{dist} to the position output p can be represented as

$$G_{\text{dist}} = \frac{p(s)}{F_{\text{dist}}(s)} = \frac{\frac{1}{m} G_4 G_5}{1 + \frac{1}{m} C_3 (C_4 + s) G_a G_4 G_5} = \frac{G_4 G_5}{m + C_3 (C_4 + s) G_a G_4 G_5} \tag{22}$$

which involves the velocity controller C_3, position controller C_4, transfer functions G_4 and G_5, and the angle loop transfer function G_a. The transfer functions G_4 and G_5 are both known from Fig. 12, so as the controllers C_3 and C_4, which have determined by well tuning and their parameters are shown in Table I. The angle loop response G_a, according to (19), is dependent on the known angle controller C_2 shown in Table I, G_3, which is an integrator from Fig. 12, and the angular rate loop G_r. We could further break down G_r as in (18), but in practice, we identify G_r directly from real flight data to obtain higher model accuracy. According to the structure of G_r in (18), it has three poles and one zero and their values are identified through the MATLAB system identification toolbox. The resultant model is

$$G_r = \frac{-23.8672s + 35879}{s^3 + 51.6\,s^2 + 2017.1s + 43762}. \tag{23}$$

Fig. 13 shows the roll rate command, which excites the roll dynamics, the measured roll rate data, and the predicted output from the identified model G_r. As can be seen, the identified

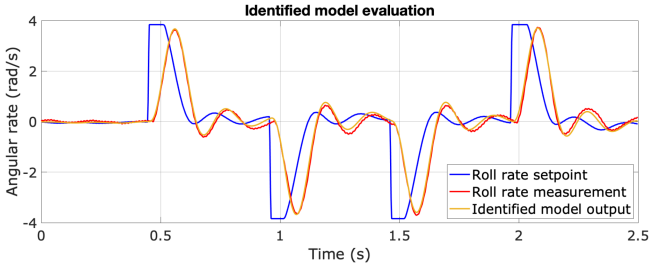

Fig. 13. Identified model evaluation.

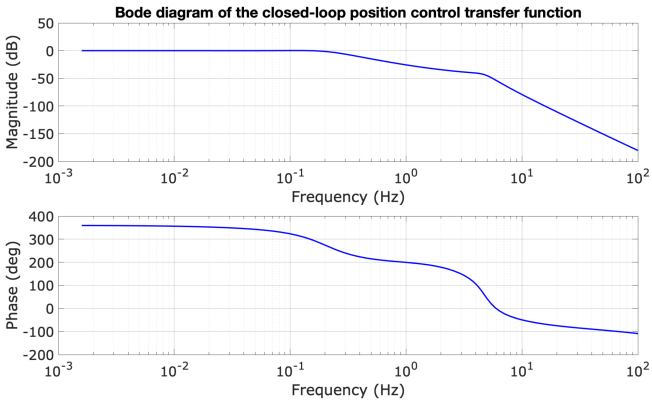

Fig. 14. Bode diagram of the closed-loop position control transfer function.

model output highly matches the actual roll rate feedback data, indicating the accuracy of the predicted dynamics of the closed-loop roll rate control system.

Once G_r and all outer loop controllers C_2, C_3, and C_4 (shown in Table I) are determined, the G_p and G_{dist} can be finally obtained as equations (24), (25) shown at the bottom of this page.

The external disturbance response bode diagram of G_p and G_{dist} is shown in Figs. 14 and 15, respectively. As shown in Fig. 15, the external disturbance force can be attenuated in the whole frequency band and the most sensitive frequency of disturbance is around 0.13 Hz with the magnitude of -2.37 dB.

C. Disturbance Test

To verify the quality of the position control loop and the robustness of the Gemini II in presence of disturbances, a poking test and a wind disturbance test are conducted.

1) Poking: With the motion capture system providing position feedback, Gemini II hovers at a fixed point in space and was hit ten times from three different angles, as shown in Fig. 16.

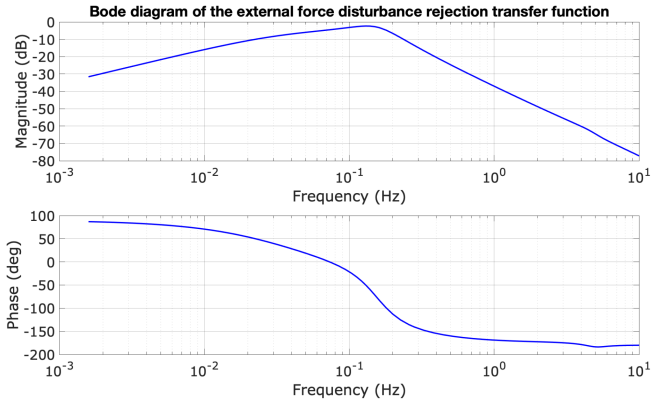

Fig. 15. Bode diagram of the external force disturbance rejection transfer function.

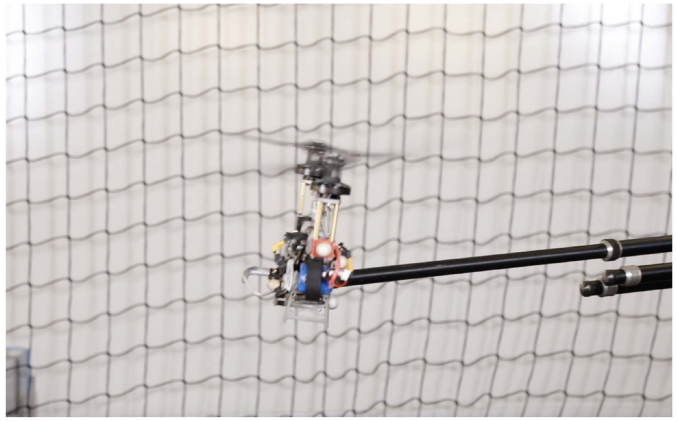

Fig. 16. Gemini II poking test.

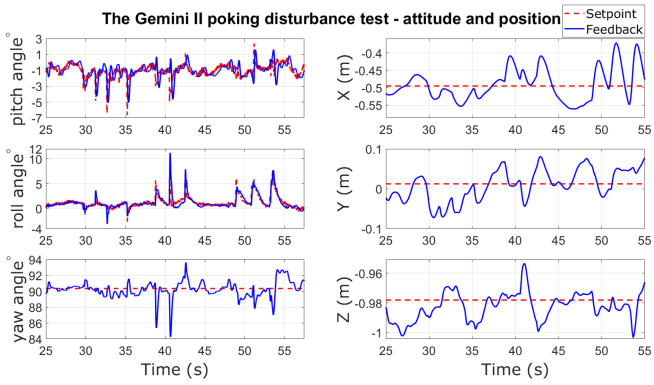

Fig. 17. Gemini II attitude and position setpoint vs. feedback during the poking test.

$$G_p = \frac{-58.95\,s^3 + 88090\,s^2 + 797500s + 177200}{s^7 + 51.61\,s^6 + 2017\,s^5 + 43390\,s^4 + 559100\,s^3 + 927500\,s^2 + 984000s + 177200} \tag{24}$$

$$G_{\text{dist}} = \frac{0.5495\,s^5 + 28.36\,s^4 + 1108\,s^3 + 23870\,s^2 + 256300\,s}{s^7 + 51.61\,s^6 + 2017\,s^5 + 43420\,s^4 + 517300\,s^3 + 509600\,s^2 + 540700s + 97390}. \tag{25}$$

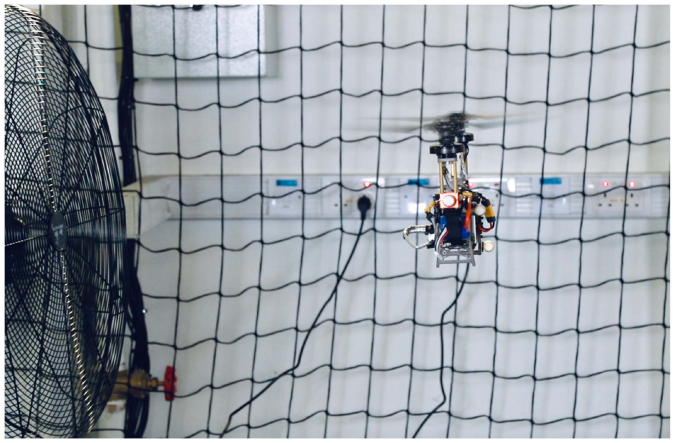

Fig. 18. Gemini II wind disturbance test.

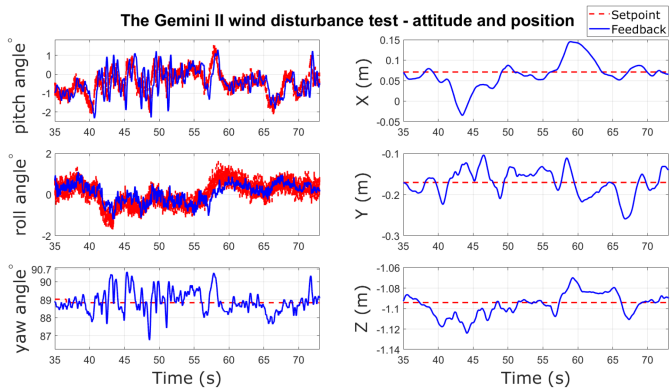

Fig. 19. Gemini II attitude and position setpoint versus feedback during the gust wind disturbance test.

Fig. 20. Gemini II following a "3-D Figure 8" pattern trajectory.

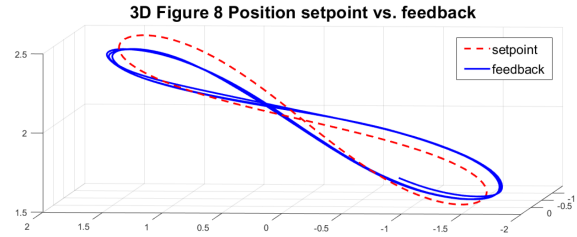

Fig. 21. "3-D Figure 8" trajectory track setpoint versus feedback.

As shown in flight data in Fig. 17, the first four hits were firmly poked at the front of the aircraft, i.e., the x-axis of the world frame. From 29 to 36 s, four consecutive hits result in four peaks on the pitch angle, ranging from 3 to 5 degrees, and were all recovered quickly. Notice that each poking also makes about 5 cm displacement on the x-direction of the world frame, and all of them were recovered within half a second.

The following three firm pokes were made on the front of the right side body, in order to test its yaw disturbance rejection performance. During the actual testing, the first two hits made between 38 and 41 s results in spikes on both yaw and roll, and the last hit made on 43 s only pushed the roll to tilt instead of having an impact on the yaw as well. From the data, we can see that both yaw and roll recovered quickly as well.

The last three hits were gentle pushes made on the center of the right-side body. The purpose of the last three hits is to test the roll attitude control ability. From 48 to 55 s, three even pushes were made, resulting in 5–10 cm displacement on the x-direction world frame as well as 5 degrees tilt on the roll angle. Each displacement disturbance was recovered within half a second. The success of this experiment marks the robustness of the controller.

2) Wind Disturbance: When the UAVs are deployed in the field, gust wind will cause complicated aerodynamic disturbances to the UAV body and the propellers. Since Gemini II uses similar differential rotation speed to control the pitch as that of the quadcopters, which has been extensively studied, the disturbance rejection performance on the roll is of particular interest to us. In order to simulate wind disturbance on the roll, Gemini II is tested at hovering where two electric fans provide operating wind speed ranging from 4.5 to 5 m/s. As shown in Fig. 18, the direction of the wind blows along the x-axis direction of the world frame, hitting on the left side of the vehicle. Fig. 19 shows the attitude and position control performance.

At first, the Gemini II was hovering at a fixed point. The electric fan was turned ON at 37 s and turned OFF at 57 s. The fan came into a complete stop at 70 s. The roll attitude data clearly shows a 1-degree disturbance while the fan got turned ON and OFF. During fan operation, disturbances of a similar frequency got reflected on the yaw and pitch angle. The response time on both pitch and roll channels is usually within 0.35 s, and the overall attitude control quality is good.

The ON and OFF of the gusting wind are responsible for the -10 and 7 cm position drift on x at 43 and 58 s, respectively. The position drift on the y- and z-axes is within 8 and 3 cm, respectively, which are within a reasonable range.

During the gust wind test, both attitude and position loops show good rejection to disturbance, indicating the robustness of the complete UAV system.

D. Trajectory Tracking Following a "3-D Figure 8" Pattern

In order to test the maneuverability and trajectory tracking performance of Gemini II, we challenged it to fly following a "3-D Figure 8" pattern, as shown in Figs. 20 and 21. Velocity and position with respect to time are shown in Fig. 22. It indicates that the lag between the setpoint and feedback is 1

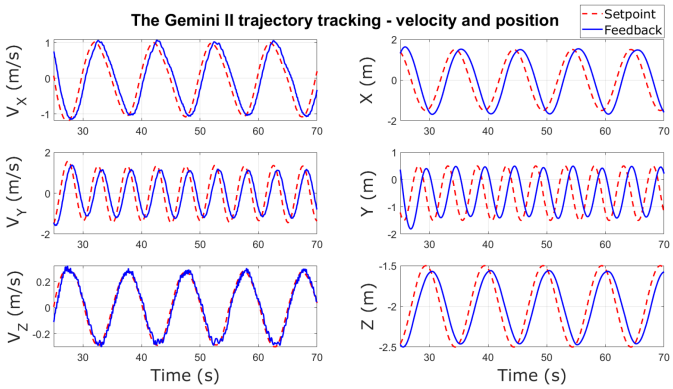

Fig. 22. Gemini II velocity and position setpoint versus feedback while following a "3-D Figure 8" pattern.

and 0.65 s, respectively. The success of the trajectory tracking validates the feasibility and performance of the novel bi-copter design.

V. Discussion

Even though Froude scaling of aircraft systems shows that the dynamics are insensitive to the gross scale of the aircraft [27], in practice, rotor rotation-dependent vibration will be unavoidably generated due to the asymmetry of the hub mechanism. This phenomenon will be more severe as the A in the throttle command increases, body length H or L increases, or the inertia of the swashplate-less mechanism increases. The vibration can potentially affect the accuracy of the flight controller IMU sensor, or even cause resonance between the two motors and damage the UAV body. Adopting a spring-damper mechanism or rubber buffer can alleviate such a problem.

VI. Conclusion

This article proposed a novel servoless bi-copter that uses a cyclic blade pitch control technique. The design, implementation details, modeling, and control are presented. Various flight and disturbance tests proved its ability to carry a heavy payload, and stably hover while subject to various disturbances. Our prototype, Gemini II, proved the feasibility of the bi-copter adopting a cyclic blade pitch control technique to achieve roll and yaw control without depending on heavy and expensive servo motors. In the future, we will conduct more quantitative analysis on the modeling of the propulsion system, improve the flight performance more by using more advanced control techniques such as model predictive control and robust control, increase swashplate-less mechanism efficiency by reducing its aerodynamic resistance, etc. In addition, we will use the LiDAR SLAM to provide position feedback, add planning algorithms to the platform, and perform autonomous flight tasks.

Acknowledgment

The authors would like to thank DJI for support, M. Huang for prototyping and manufacturing the fuselage, T-MOTOR for providing product CAD files, and Y. Li for providing Gemini mini's transfer function.

References

[1] Y. Khosiawan and I. Nielsen, "A system of UAV application in indoor environment," *Prod. Manuf. Res.*, vol. 4, no. 1, pp. 2–22, 2016.
[2] F. Nex and F. Remondino, "UAV for 3D mapping applications: A review," *Appl. Geomatics*, vol. 6, no. 1, pp. 1–15, 2014.
[3] V. Baiocchi, D. Dominici, and M. Mormile, "UAV application in post-seismic environment," *Int. Arch. Photogrammetry, Remote Sens. Spatial Inf. Sci.*, vol. 1, pp. 21–25, 2013.
[4] K. Ivushkin *et al.*, "UAV based soil salinity assessment of cropland," *Geoderma*, vol. 338, pp. 502–512, 2019.
[5] J. Senthilnath, M. Kandukuri, A. Dokania, and K. Ramesh, "Application of UAV imaging platform for vegetation analysis based on spectral-spatial methods," *Comput. Electron. Agriculture*, vol. 140, pp. 8–24, 2017.
[6] J. Lin, L. Wang, F. Gao, S. Shen, and F. Zhang, "Flying through a narrow gap using neural network: An end-to-end planning and control approach," *IEEE/RSJ Int. Conf. Intell. Robot. Syst. (IROS)*, pp. 3526–3533, 2019, doi: 10.1109/IROS40897.2019.8967944.
[7] D. Falanga, E. Mueggler, M. Faessler, and D. Scaramuzza, "Aggressive quadrotor flight through narrow gaps with onboard sensing and computing using active vision," in *Proc. IEEE Int. Conf. Robot. Automat.*, 2017, pp. 5774–5781.
[8] V. Riviere, A. Manecy, and S. Viollet, "Agile robotic fliers: A morphing-based approach," *Soft Robot.*, vol. 5, no. 5, pp. 541–553, 2018.
[9] N. Bucki and M. W. Mueller, "Design and control of a passively morphing quadcopter," in *Proc. IEEE Int. Conf. Robot. Automat.*, 2019, pp. 9116–9122.
[10] D. Falanga, K. Kleber, S. Mintchev, D. Floreano, and D. Scaramuzza, "The foldable drone: A morphing quadrotor that can squeeze and fly," *IEEE Robot. Automat. Lett.*, vol. 4, no. 2, pp. 209–216, Apr. 2019.
[11] J. Leishman, *Principles of Helicopter Aerodynamics*. Cambridge, U.K.: Cambridge Univ. Press, 2006.
[12] Y. Qin, W. Xu, A. Lee, and F. Zhang, "Gemini: A compact yet efficient bi-copter UAV for indoor applications," *IEEE Robot. Automat. Lett.*, vol. 5, no. 2, pp. 3213–3220, Apr. 2020.
[13] "Boeing: H-47 Chinook," Boeing. Accessed: Mar 2, 2022. [Online]. Available: https://www.boeing.com/defense/ch-47-chinook/#/technical-specifications
[14] A. Sanchez, J. Escareno, O. Garcia, and R. Lozano, "Autonomous hovering of a noncyclic tiltrotor UAV: Modeling, control and implementation," *IFAC Proc. Volumes*, vol. 41, no. 2, pp. 803–808, 2008.
[15] C. Papachristos, K. Alexis, G. Nikolakopoulos, and A. Tzes, "Model predictive attitude control of an unmanned tilt-rotor aircraft," in *Proc. IEEE Int. Symp. Ind. Electron.*, 2011, pp. 922–927.
[16] L. Hrečko, J. Slačka, and M. Halás, "Bi-copter stabilization based on IMU sensors," in *Proc. 20th Int. Conf. Process Control*, 2015, pp. 192–197.
[17] Q. Zhang, Z. Liu, J. Zhao, and S. Zhang, "Modeling and attitude control of bi-copter," in *Proc. IEEE Int. Conf. Aircr. Utility Syst.*, 2016, pp. 172–176.
[18] F. Gonçalves, J. R. Bodanese, G. Donadel, J. Raffo Normey-Rico, and L. Becker, "Small scale UAV with birotor configuration," in *Proc. Int. Conf. Unmanned Aircr. Syst.*, 2013, pp. 761–768.
[19] Y. Li, Y. Qin, W. Xu, and F. Zhang, "Modeling, identification, and control of non-minimum phase dynamics of bi-copter UAVs," in *Proc. IEEE/ASME Int. Conf. Adv. Intell. Mechatronics*, 2020, pp. 1249–1255.
[20] Y. Qin, Y. Li, X. Wei, and F. Zhang, "Hybrid aerial-ground locomotion with a single passive wheel," in *Proc. IEEE/RSJ Int. Conf. Intell. Robots Syst.*, 2020, pp. 1371–1376.
[21] K. Siddhardha, "A novel bi-rotor configuration and its control," *IFAC-PapersOnLine*, vol. 51, no. 1, pp. 456–461, 2018.
[22] G. Özdoğan and K. Leblebicioğlu, "Modeling and control of a heavy-lift helicopter consisting of large and small tilting rotors," in *Proc. 6th Int. Conf. Control Eng. Inf. Technol.*, 2018, pp. 1–6.
[23] K. Åström, "Fundamental limitations of control system performance," in *Communications, Computation, Control, and Signal Processing*. Germany: Springer, 1997.
[24] J. Paulos and M. Yim, "An underactuated propeller for attitude control in micro air vehicles," in *Proc. IEEE/RSJ Int. Conf. Intell. Robots Syst.*, 2013, pp. 1374–1379.
[25] J. Paulos and M. Yim, "Flight performance of a swashplateless micro air vehicle," in *Proc. IEEE Int. Conf. Robot. Automat.*, 2015, pp. 5284–5289.

[26] J. Paulos and M. Yim, "Cyclic blade pitch control without a swashplate for small helicopters," *J. Guid. Control Dyn.*, vol. 41, no. 3, pp. 689–700, 2018.
[27] J. J. Paulos and M. Yim, "Scalability of cyclic control without blade pitch actuators," in *Proc. AIAA Atmospheric Flight Mechanics Conf.*, 2018, pp. 1–18.
[28] J. Paulos, B. Caraher, and M. Yim, "Emulating a fully actuated aerial vehicle using two actuators," in *Proc. IEEE Int. Conf. Robot. Automat.*, 2018, pp. 7011–7016.
[29] D. Mellinger and V. Kumar, "Minimum snap trajectory generation and control for quadrotors," in *Proc. IEEE Int. Conf. Robot. Automat.*, 2011, pp. 2520–2525.
[30] X. Lyu, H. Gu, J. Zhou, Z. Li, S. Shen, and F. Zhang, "A hierarchical control approach for a quadrotor tail-sitter VTOL UAV and experimental verification," in *Proc. IEEE/RSJ Int. Conf. Intell. Robots Syst.*, 2017, pp. 5135–5141.

Youming Qin received the B.S. degree in electrical engineering, in 2018, from the Virginia Polytechnic Institute and State University, Blacksburg, VA, USA. He is currently working toward the Ph.D. degree in mechanical engineering with the University of Hong Kong, Hong Kong.

His research interests include mechatronics and robotics, VTOL and multirotor UAV system design, autonomous vehicles, and control.

Nan Chen received the B.Eng. degree in automation and the M.Eng. degree in control theory and control engineering from the Shenzhen University, Shenzhen, China, in 2015 and 2019, respectively. He is currently working toward the Ph.D. degree in UAV design, control, and SLAM application with the Department of Mechanical Engineering, University of Hong Kong, Hong Kong, China.

His research interests include unmanned aerial vehicles design and control.

Yixi Cai received the B.Sc. degree in automation from the School of Automation Science and Electrical Engineering, Beihang University, Beijing, China, in 2020. He is currently working toward the Ph.D. degree in system identification, sensor fusion, and mapping with the Department of Mechanical Engineering, University of Hong Kong, Hong Kong, China.

His research interests include system identification, sensor fusion, and advanced controller design on unmanned aerial vehicles.

Wei Xu received the B.S. and M.S. degrees in aerial vehicle design from the Beihang University, Beijing, China, in 2015 and 2018, respectively. He is currently working toward the Ph.D. degree in control and SLAM with the Department of Mechanical Engineering, University of Hong Kong, Hong Kong, China.

His research interests include advanced aerial robots control, sensor fusion, and LiDAR SLAM.

Fu Zhang (Member, IEEE) received the B.E. degree in automation from the University of Science and Technology of China, Hefei, China, in 2011, and the Ph.D. degree in mechanical engineering from the University of California, Berkeley, CA, USA, in 2015.

Since 2018, he has been with the University of Hong Kong, Hong Kong, where he is currently an Assistant Professor in Mechanical Engineering. His research interests include mechatronics and robotics, with a focus on UAV design, control, and LiDAR-based navigation.